

Article

PEO Infiltration of Porous Garnet-Type Lithium-Conducting Solid Electrolyte Thin Films

Aamir Iqbal Waidha^{1,2}, Vanita Vanita^{1,2} and Oliver Clemens^{1,2,*} 

¹ Materials Synthesis Group, Institute for Materials Science, University of Stuttgart, Heisenbergstraße 3, 70569 Stuttgart, Germany; aamir.waidha@imw.uni-stuttgart.de (A.I.W.); vanita@imw.uni-stuttgart.de (V.V.)

² Fachgebiet Materialdesign durch Synthese, Institut für Materialwissenschaft, Technische Universität Darmstadt, 64287 Darmstadt, Germany

* Correspondence: oliver.clemens@imw.uni-stuttgart.de; Tel.: +49-711-6855-1933

Abstract: Composite electrolytes containing lithium ion conducting polymer matrix and ceramic filler are promising solid-state electrolytes for all solid-state lithium ion batteries due to their wide electrochemical stability window, high lithium ion conductivity and low electrode/electrolyte interfacial resistance. In this study, we report on the polymer infiltration of porous thin films of aluminum-doped cubic garnet fabricated via a combination of nebulized spray pyrolysis and spin coating with subsequent post annealing at 1173 K. This method offers a simple and easy route for the fabrication of a three-dimensional porous garnet network with a thickness in the range of 50 to 100 μm , which could be used as the ceramic backbone providing a continuous pathway for lithium ion transport in composite electrolytes. The porous microstructure of the fabricated thin films is confirmed via scanning electron microscopy. Ionic conductivity of the pristine films is determined via electrochemical impedance spectroscopy. We show that annealing times have a significant impact on the ionic conductivity of the films. The subsequent polymer infiltration of the porous garnet films shows a maximum ionic conductivity of $5.3 \times 10^{-7} \text{ S cm}^{-1}$ at 298 K, which is six orders of magnitude higher than the pristine porous garnet film.

Keywords: lithium ion batteries; garnet; thin films; composite electrolyte



Citation: Waidha, A.I.; Vanita, V.; Clemens, O. PEO Infiltration of Porous Garnet-Type Lithium-Conducting Solid Electrolyte Thin Films. *Ceramics* **2021**, *4*, 421–436. <https://doi.org/10.3390/ceramics4030031>

Academic Editors: Gilbert Fantozzi and Giuseppe Viola

Received: 23 April 2021

Accepted: 13 July 2021

Published: 23 July 2021

Publisher's Note: MDPI stays neutral with regard to jurisdictional claims in published maps and institutional affiliations.



Copyright: © 2021 by the authors. Licensee MDPI, Basel, Switzerland. This article is an open access article distributed under the terms and conditions of the Creative Commons Attribution (CC BY) license (<https://creativecommons.org/licenses/by/4.0/>).

1. Introduction

All solid-state Li-ion batteries (ASSLBs) with metallic lithium (Li) as the negative electrode are potential alternatives to conventional Li-ion batteries, which contain carbon-based anodes and liquid electrolytes [1–3]. The use of metallic Li as an anode gives rise to the high energy density of the Li-ion battery, since it offers an order of magnitude higher capacity as compared to the conventional carbon-based anodes currently being employed (3860 mAh g^{-1} vs. 372 mAh g^{-1}) [4,5] at a lower anode potential. On the other hand, the use of solid electrolytes can reduce the long-standing safety issues of hydrocarbon-containing liquid electrolytes employed in batteries with liquid electrolytes, i.e., flammability, leakage, dendrite growth, etc. [2,6], and provide an alternative to room-temperature ionic liquids (RTIL) [7], which can be expensive to fabricate.

Both inorganic and polymer-based solid electrolytes (the latter abbreviated as PSEs) have gathered widespread interest over the years for their application in ASSLBs [4,6,8,9]. PSEs are comprised of a polymer matrix that dissolves Li salts. A variety of PSEs, such as polyvinylidene fluoride (PVDF), polyacrylonitrile (PAN), poly(ethyl carbonate) (PEC), poly(methyl methacrylate) (PMMA) and polyethylene oxide (PEO), have been of interest [10]. Among them, PEO is considered a promising host due to its commercial availability, low cost and non-toxicity. PEO is a polyether with the chain composed of $(\text{CH}_2\text{-CH}_2\text{-O})_n$ structural units. PEO is particularly interesting due to its excellent lithium-salt solubility, superior flexibility and adhesivity, which can be beneficial for reducing interfacial resistance [9,11] by forming an even

contact with the metallic Li anode and can also adapt to the volume changes of the active electrode materials during battery cycling. However, it lacks mechanical strength, which makes it susceptible to dendrite growth in combination with metallic Li anodes [9,11–13]. Further, PEO-based electrolytes show low Li-ion conductivity (10^{-7} – 10^{-6} S cm $^{-1}$) [10], low Li-ion transference number (i.e., 0.22 for PEO:LiTFSI), instability against metallic lithium anodes and a comparably small electrochemical stability window (4.25 V vs. Li $^{+}$ /Li) [11,14]. The low Li-ion conductivity in PEO is known to be a result of the coexistence of crystalline and amorphous phases. It is widely believed that amorphous PEO offers higher Li-ion conductivity compared to that of crystalline PEO [15]. Although alternative approaches to improve polymer conductivity by using different conductive salts have been explored, e.g., via the use of room-temperature ionic liquids (RTILs), these are expensive compared to conventionally used Li-containing salts [7]. Therefore, other methods for reducing PEO crystallinity for conductivity enhancement are of interest.

On the other hand, inorganic solid electrolytes based on oxides have been within the focus of recent research [4,6,16–20]. Oxide-based garnets (Li $_7$ La $_3$ Zr $_3$ O $_{12}$ (LLZO)) have been considered due to their high intrinsic Li-ion conductivity (1.3×10^{-3} S cm $^{-1}$) [6], their wide electrochemical stability window (>6 V vs. Li/Li $^{+}$) [21] and their compatibility with the Li metal anode [6,22–24]. However, due to their high brittleness, achieving good contact with metallic Li is often a challenge, which results in increased interfacial resistances at the Li/LLZO interface and uneven stripping/plating of lithium, which can result in dendrite formation at high current densities [2,6,18]. Further, they are also known to be highly sensitive towards moisture and CO $_2$, which can result in the formation of Li $_2$ CO $_3$ via an intermediate LiOH phase on the particle surface [25,26].

In order to overcome the drawbacks of both organic and inorganic electrolytes, an alternative strategy of mixing the two into composite electrolytes (CEs) might result in harnessing the advantages of both systems while limiting the disadvantages. Such CEs have already been investigated in recent years [27–34]. CEs are comprised of polymer matrix and dispersed ceramic filler [35,36] and offer higher Li-ion conductivity (6.24×10^{-5} S cm $^{-1}$ at 298 K) [37], higher mechanical strength, an enhanced electrochemical window (5 V vs. Li/Li $^{+}$) [35] and higher Li-ion transference number (0.46) [14] than the pure polymers [38,39]. Compared to the pure ceramic-based electrolytes, CEs offer higher flexibility and softness, thus forming a smooth and even contact with the Li metal at the Li/CE interface [37], which can result in even Li stripping/plating, thus preventing lithium dendrite formation [14]. So far, the research has been focused on the polymer rich composites, wherein the dispersion of the low weight percentages of ceramic filler has been known to increase the conductivity and Li-ion transference number [14]. However, the room temperature conductivities of such CEs are still approximately two orders of magnitude too low for their application in room temperature [6] ASSLB. Since the sintered ceramic LLZO is known to offer high conductivities ($\sim 10^{-3}$ S cm $^{-1}$) [6], an alternative strategy therefore could be the use of ceramic-rich CEs. However, such high conductivities are not observed in the CEs containing high weight percentages of ceramic filler dispersion, due to high grain boundary impedances towards Li-ion transport. To mitigate the high grain boundary impedances due to ceramic filler dispersion, an alternative strategy of forming a continuous and sintered porous three-dimensional garnet network followed by its infiltration with the Li-ion conducting polymer can prove to be advantageous in terms of conductivity enhancements in these CEs for their application in ASSLBs. A porous sintered network would in principle lower the ceramic/ceramic boundary resistances and promote Li-ion conductivity within the garnet framework as opposed to the ceramic dispersion in the ceramic-rich CEs, thus enhancing the overall ionic conductivity. Recently, the group of Wachsman has shown that porous electrolyte architectures can be realized in principle and are scalable for their application in solid state batteries [40]. The fabrication method used by them results in thin films with large particle sizes and low porosity, which within an infiltration approach would result in small garnet/PEO interfacial contact areas. The ceramic/polymer interface is considered to be crucial for conductivity enhancement

in CEs [35,41]. Overall, the fabrication of such networks has not been investigated in much detail, and different fabrication techniques and microstructures can provide different functional properties.

In this article, we report for the first time the synthesis and polymer infiltration of porous garnet thin films prepared by the combination of nebulized spray pyrolysis (NSP) and spin coating. Initially garnet powders were synthesized via the NSP route followed by film fabrication via spin coating and sintering. NSP processed powders offer the advantage of reduced sintering times and temperatures in order to obtain the desired garnet phase with a highly porous microstructure, which significantly lowers the ceramic density (47–55%) compared to that of theoretical density [42], a precondition to synthesize porous ceramic materials. Phase analysis is carried out by Rietveld analysis of the X-ray powder diffraction (XRD) data. The porous garnet thin films are then infiltrated by PEO+LiTFSI solution via the drop technique. Scanning electron microscopy (SEM) is used to obtain an understanding about the microstructure and success of infiltration. The conductivity measurements of the mere garnet film and the infiltrated garnet films are carried out using electrochemical impedance spectroscopy (EIS). The results show that polymer infiltration leads to increased ionic conductivity in the infiltrated garnet thin films along with the additional lithium ion transport pathways in the infiltrated films.

2. Materials and Methods

For the synthesis of nano- to microcrystalline powders of $\text{Li}_{6.49}\text{Al}_{0.17}\text{La}_3\text{Zr}_2\text{O}_{12}$, the NSP method was used. A three step process was used for the preparation of water based solution: (i) First, the Zr precursor ($\text{Zr}(\text{C}_5\text{H}_7\text{O}_2)_4$, ABCR, 98%) was dissolved in a small volume of methanol; (ii) the Li, La and Al nitrate-based salts were then added to this methanolic solution (LiNO_3 , Sigma Aldrich, 99.99%, $\text{La}(\text{NO}_3)_3 \cdot 6\text{H}_2\text{O}$, Alfa Aesar, 99.9%, $\text{Al}(\text{NO}_3)_3 \cdot 9\text{H}_2\text{O}$, Merck, 98.5%); (iii) finally, deionized water was added to this solution in order to maintain overall desired concentration of 0.1 mol L^{-1} . A water to methanol volume ratio of 20:1 was used. The obtained solution was then subjected to magnetic stirring for 1 h in order to produce a homogenous transparent solution. In order to compensate the Li loss in the subsequent high temperature sintering processes, 50% excess of Li precursor was used. This precursor solution was then injected at a constant flow rate of 100 mL h^{-1} into a glass chamber using a syringe pump (TSI), where the nebulization took place using an ultrasonic generator (Dr. Hielscher UM20-1.6 MHz). The mist of the precursor solution was then transferred into a hot-wall reactor using a constant flow of oxygen (3 SLM (standard liter per minute) flow rate controlled by an MKS mass flow controller (MFC)). The whole process was carried at a constant pressure of 900 mbar maintained using a Baraton absolute pressure gauge and a butterfly valve connected to a backing pump. The powders were synthesized at a temperature of 1173 K and collected by using a filter-based collector, which was maintained at 393 K to prevent water vapor condensation (referred to as “as-synthesized” in the following). As-synthesized powders were subsequently sintered at 1173 K for 3 h in ambient air. A constant heating rate of 6 K min^{-1} and a cooling rate of 6 K min^{-1} were used (referred to as “sintered” in the following). This experimental procedure followed has already been reported by us in several other reports [33,43,44] and could be well reproduced here.

To obtain the garnet thin films, as-synthesized NSP powders were utilized in order to obtain the porous garnet films. As-synthesized NSP powders were weighed (0.100 mg) and stirred in 400 μL of TBE (1,1,2,2-tetrabromoethane) for 30 min; this high-density solvent was necessary in order to obtain a dispersion that was stable for subsequent treatment. The solution was then spin coated onto the copper substrate using a three-step spinning program based on the following rotating steps: 425 rpm for 1 min, 325 rpm for 0.6 min and 225 rpm for 2 min. The as-obtained films were then sintered at 1073 K for 60 min at the heating and cooling rate of 3 K/min in the tube furnace under the flow of argon. The films were then transferred to an Ar-filled glove box for the subsequent steps and to limit the exposure to the ambient atmosphere. This is important since garnets are known to be

susceptible towards moisture, which can result in the formation of Li_2CO_3 on the garnet surface [45] and contribute towards the interfacial impedances at the garnet/PEO interface.

For the infiltration of the porous garnet thin films, PEO+LiTFSI (bis(trifluoromethane) sulfonimide) containing solutions was used. The solution was prepared by first dissolving 0.1 g of LiTFSI in 5 mL of acetonitrile. After stirring for 15 min, 0.2 g of PEO were added to the solution and stirred until PEO was completely dissolved into the solution. The solution was then poured drop-wise onto the garnet thin film using a micropipette. The dropwise pouring was repeated several times (20–30 times), and the films were dried in a vacuum furnace for 12 h at 323 K before carrying out impedance measurements. We emphasize here that the amount of PEO+LiTFSI used within the solution is of high importance. Increasing the PEO amount in the solution was found to result in a solution with higher viscosity, which resulted in PEO depositing on the surface of the garnet film. The infiltration procedure was found to be reproducible for the thin films reported here.

Room temperature XRD patterns of the various samples were recorded on a Bruker D8 diffractometer using Bragg–Brentano geometry with a fine focusing X-ray tube with $\text{Cu K}_{\alpha 1,2}$ radiation. A VANTEC detector (3° opening) and a fixed divergence slit (0.3°) were used. The total scan time was set to 1 h for the angular range between 10° and 80° 2θ at a step size of 0.0066° . The Rietveld method was used to carry out the structural refinement and phase analysis of the XRD patterns using the TOPAS 5 program (Bruker AXS, Karlsruhe, Germany) [46]. Using a reference scan of LaB6 (NIST 660a), the instrumental intensity distribution was calculated empirically within a fundamental parameter approach [47], and the micro-structural parameters were adjusted to adjust the peak morphologies for the XRD data. To account for absorption adjustments, an overall isotropic value was refined, which was constrained to be identical for all atoms in all phases.

Alternating current (AC) electrochemical impedance spectroscopy was carried out to characterize the conductivity of the pure and the infiltrated garnet films. The films were sputtered with a thin layer of gold on the top for electronic contacting, whereas the Cu substrates serve as the bottom contact. The measurements were carried out within a through-plane geometry. Films were then placed inside a JANIS STVP-200-XG cryostat, which was operated under a static helium atmosphere of 1 bar pressure. LLZO films were investigated in the temperature range of 298 K to 473 K, whereas the infiltrated films were investigated in the temperature range of 298 K to 328 K due to the higher conductivity. Impedance measurements were recorded using a Solartron 1260 frequency response analyzer, applying an AC signal of 100 mV amplitude with the frequency ranging from 1 MHz to 100 mHz. Fitting of the data was performed using the Z-view program [48].

The authors would like to emphasize that attempts to prepare and characterize pure and infiltrated films were performed on at least three films independently. Film compositions were highly reproducible with insignificant (below 1–2%) changes of phase compositions. Though some fluctuations of film thickness in the order of ~10–30% and also smaller fluctuations in conductivity could occur (i.e., comparing different infiltrated films, e.g., in the range of $10^{-6.0}$ – $10^{-6.2}$ S cm^{-1} , see Figure S1 in the Supplementary Information), the principle phenomenon of increased conductivity of the film after infiltration by several orders of magnitudes with the corresponding phenomenological behavior of the semicircles observed in the impedance spectra could be well reproduced between different samples.

3. Results and Discussion

3.1. X-ray Diffraction

Lithium stuffed garnets can crystallize in tetragonal ($I4_1/acd$) or cubic ($Ia-3d$) space groups depending on the Li-ion distribution within the lattice and the doping chosen [6]. The tetragonal polymorph is thermodynamically stable in the low temperature regime, whereas the cubic polymorph is stable at higher temperatures (above 673 K, depending on the impurity level) [6]. Cubic garnets are of greater interest than their tetragonal counterparts, since they are known to offer two orders of magnitude higher Li-ion conductivity. They can be stabilized via aliovalent doping (i.e., with Al^{3+}) leading to the disordered

distribution of Li-ions, thus making the material a fast Li-ion conductor [6]. Therefore, within this study, cubic garnets were used to prepare a 3D garnet framework backbone for the composite electrolyte thin films.

Figure 1a shows the room temperature X-ray diffraction patterns of the as-synthesized NSP powders of cubic Al-doped garnet powders. Rietveld fit (Figure 1a) of the powder X-ray diffractogram of as-synthesized NSP powders showed that the powders were mainly composed of fluorite type $\text{La}_2\text{Zr}_2\text{O}_7$ and Li_2CO_3 , which is typical of NSP-synthesized powders with this composition [43,44]. The lattice parameters of $\text{La}_2\text{Zr}_2\text{O}_7$ and Li_2CO_3 were found to be in good agreement with the previously reported values [43,44]. In order to obtain the desired garnet phase, an additional heating step is typically required. Figure 1b shows the Rietveld fit of X-ray diffraction patterns of the Al-doped cubic garnet powders. The formation of cubic garnet was observed, which is consistent with the successful incorporation of Al into garnet powders [43]. The lattice parameter of 12.9712(6) Å was calculated; from a comparison to previous composition-dependent studies [43,44] of the lattice parameter using the same synthesis method, the targeted composition of $\text{Li}_{6.49}\text{Al}_{0.17}\text{La}_3\text{Zr}_2\text{O}_{12}$ could be well deduced. Additionally, approximately 8 wt % of pyrochlore type $\text{La}_2\text{Zr}_2\text{O}_7$ was also observed, which is a common impurity phase present in garnet powders due to Li loss [44].

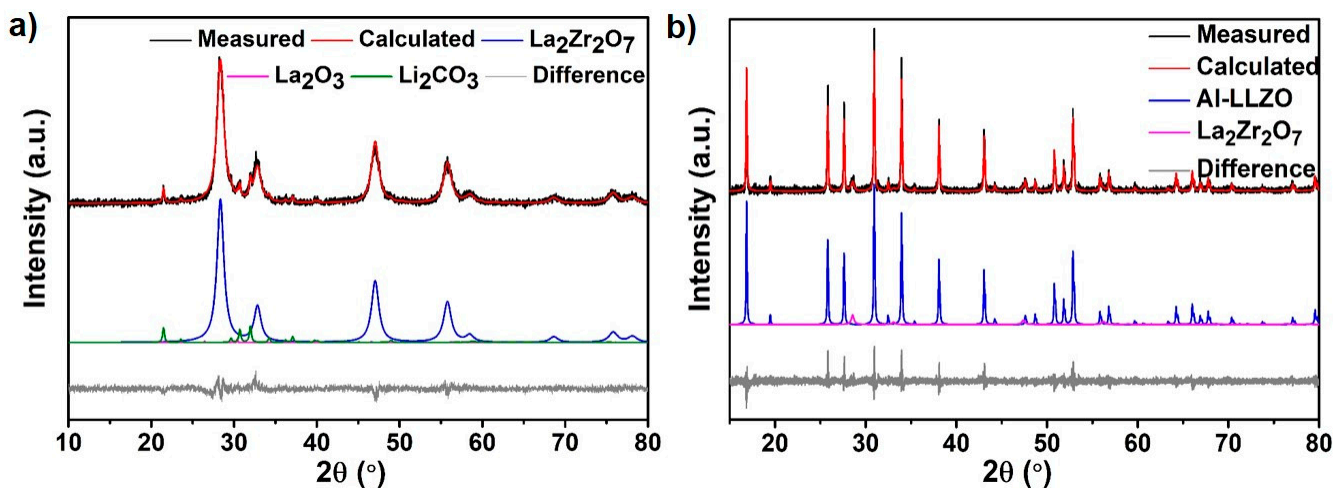


Figure 1. (a) Rietveld fit of the as-synthesized powders obtained from the NSP. (b) Rietveld fit of the X-ray diffraction pattern of Al-doped cubic garnet powders after heat treatment.

For the fabrication of porous garnet thin films via spin coating, as-synthesized NSP powders were utilized instead of the sintered powders in order to maintain the porous garnet microstructure and limit the additional sintering step, which can result in Li loss and promote the formation of the non-conducting pyrochlore phase ($\text{La}_2\text{Zr}_2\text{O}_7$) [43]. Spin coating has previously only been used for the fabrication of the dense garnet thin films [49,50]. Figure 2a shows the room temperature X-ray diffractograms of the Al-doped garnet films obtained after heat treatment at 1173 K for different times. Figure 2b shows the Rietveld fit of the Al-doped cubic garnet film sintered at 1173 K for 180 min. Other than the presence of the cubic garnet phase, an additional impurity phase of $\text{Li}_{0.5}\text{Al}_{0.5}\text{La}_2\text{O}_4$ (up to ~7.7 wt %) could also be observed. Increasing the heating time to 240 min leads to the formation of additional impurity phases (see Figure S2); therefore, for further studies, 180 min of annealing time was considered to be the optimum.

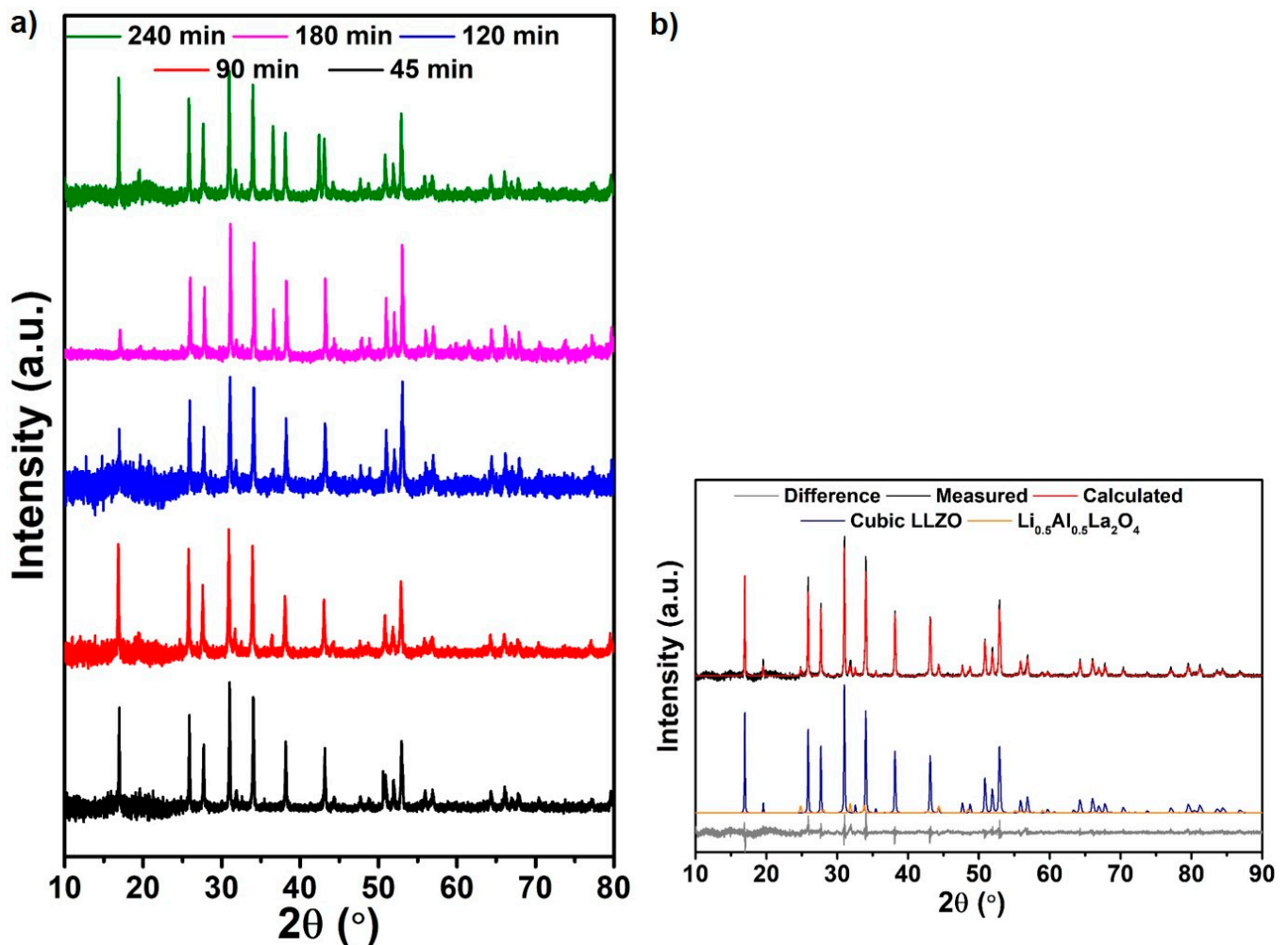


Figure 2. (a) X-ray diffraction patterns recorded for Al-doped garnet sintered at 1173 K for different durations. (b) Rietveld fit for the Al-doped LLZO annealed for 180 min at 1173 K. The increased noise at low angles originates from subtraction of the background from the air tight sample holder.

3.2. Microstructure

For the microstructural analysis, SEM micrographs were recorded and are shown in Figure 3a,b show the SEM micrograph of the as-synthesized and heat-treated garnet powders, respectively. The as-synthesized powders mainly show hollow spherical morphology with broad particle size distribution, which is typical for the powders synthesized via the NSP route [43,51,52]. As discussed previously, the as-synthesized powders mainly contain $\text{La}_2\text{Zr}_2\text{O}_7$ and Li_2CO_3 as the main phases, therefore requiring an additional heating step to obtain the garnet phase. In a previous report using the same setup, heating at 1273 K for 1 h was found to be required in order to obtain the desired garnet phase [43]. Within this study, it was found that the synthesis procedure could be further optimized, and the sintering was carried out at 1173 K for 3 h, which resulted in the formation of the Al-doped cubic garnet phase. The additional heating step significantly influenced the morphology of the powders, which tended to agglomerate via the formation of necks between the particles. However, since the heating temperature and time for the garnet synthesis via the NSP route is significantly reduced compared to that of a solid-state route, the pellets are usually porous with densities between 47% to 55% with respect to the crystallographic density [43]. Clearly, this morphology provides also a higher surface area compared to that of powders obtained from a solid-state route. This could be beneficial in CEs, as high surface area of the filler material has been shown to improve the conductivity of the CEs [29,53].

Figure 3c–f shows the top view of the Al-doped LLZO thin films annealed at different temperatures. It was found that the porous microstructure was retained, irrespective of the annealing times chosen, though they were shown to strongly influence the total ionic conductivity of the garnet thin films (see Section 3.3). The porous morphology of the garnet backbone is inherent to the NSP-synthesized powders sintered at low temperatures and times, irrespective of the ceramic composition [43,54]. This is most likely influenced by the hollow-sphere structure obtained for the as-synthesized material, which facilitates fairly high porosities and thus prohibits strong densification by sintering significantly below the material's melting temperature.

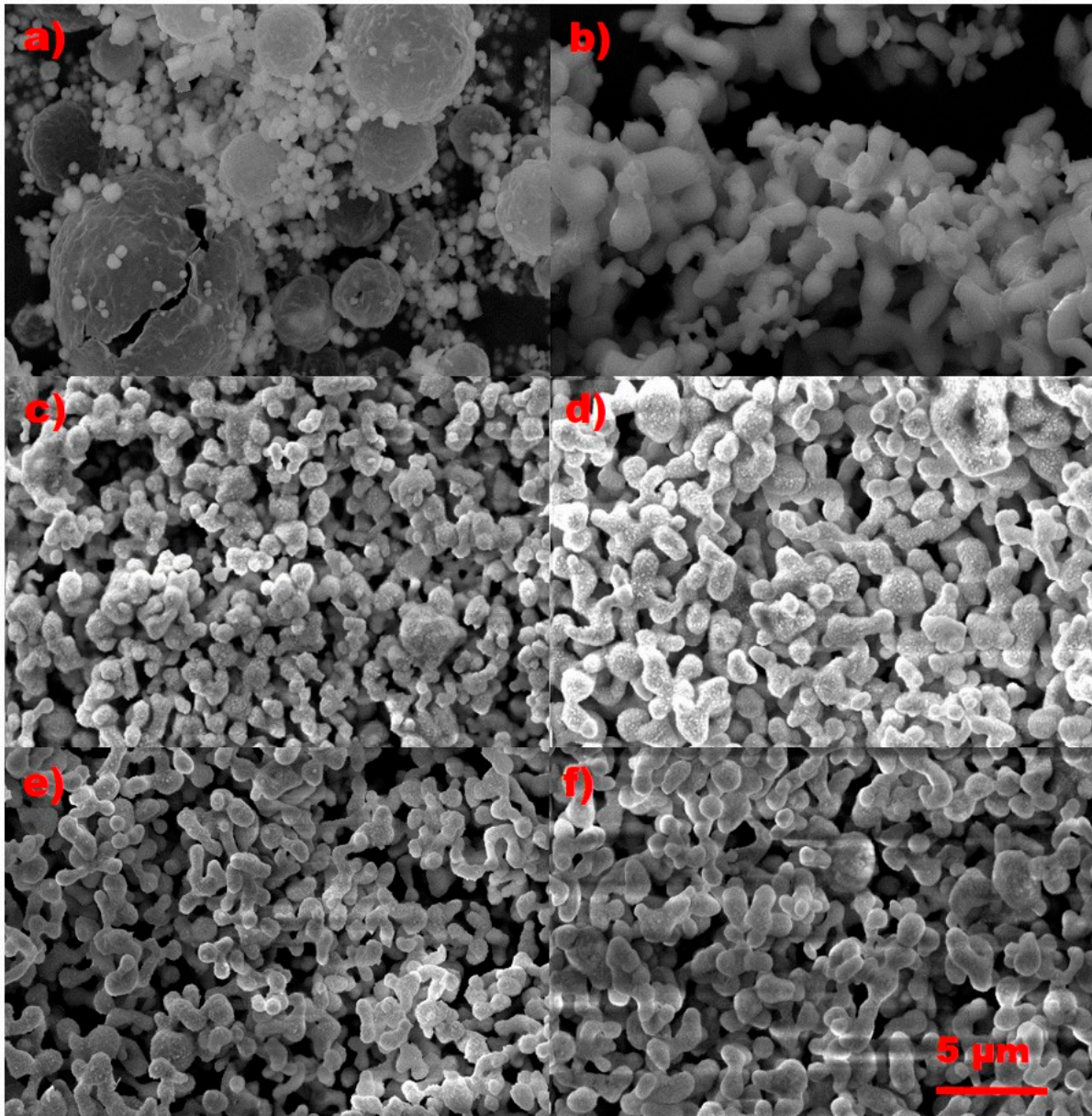


Figure 3. (a,b) Scanning electron micrograph of as-synthesized and heat treated NSP powders, respectively. (c–f) Top view of the Al-doped garnet thin films sintered at 1173 K for 60, 90, 120 and 180 min, respectively.

Initially, attempts were made to infiltrate porous pellets with a thickness of >1 mm. On this scale, it was found that only a fraction of the pore volume was accessible via an infiltration approach. Therefore, garnet thin films with a thickness ranging from 50 to 100 μm were fabricated via the spin coating method. Figure 3 shows the top view of the

heat-treated garnet thin film showing the porous garnet network (see Figure S3 for cross sectional view). This network was then infiltrated with PEO+LiTFSI containing acetonitrile solution. Figure 4a,b shows the top and the cross-sectional view of the infiltrated garnet films, respectively. This resulted in a significantly improved homogeneity and degree of infiltration as compared to a porous pellet, though a small degree of inhomogeneity could still be observed.

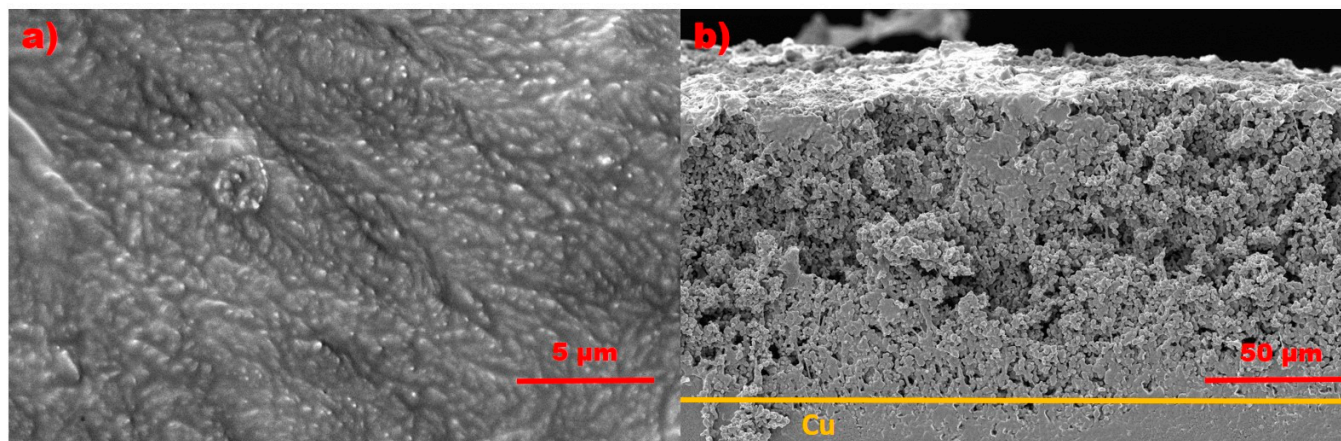


Figure 4. (a,b) Scanning electron micrograph of top and cross-sectional view of the infiltrated garnet thin film. The Cu substrate seen as the dense material in the lower part of Figure 4b.

3.3. Impedance Spectroscopy

For garnets, it is well known that the crystal structure, sintering temperatures and times play a crucial role on the obtained total Li-ion conductivity [6,42,55]. Cubic garnets are known to offer two orders of magnitude higher conductivity than their tetragonal counterparts. Although there is only a small difference between the structural arrangement within the cubic and tetragonal garnet framework of the heavy cations, it has been shown that small amounts of Al doping influence the Li vacancy density in the Li octahedral sites near the dopants, which has been shown to be key to increased conductivity [6]. The fully ordered tetragonal garnet consists of three Li sites (one tetrahedrally coordinated site Li1 (8a)), two octahedrally coordinated sites Li2 and Li3 (16f and 32g)) with a site occupancy factor of 1. For the cubic garnet, three Li sites (one tetrahedral Li1 site (24d), one octahedral Li2 site (48g/96h)) are present. The Al dopant is known to occupy the tetrahedral site and leads to significant disorder in the Li sub-lattice due to the electrostatic effects, which splits the octahedral Li2 site into two 96h sites being separated by the 48g site. The active vacancy density in this group is known to contribute towards the increased Li-ion conductivity. Further, it has been shown that the density and the microstructure of the garnets synthesized via different synthesis and compaction methods have a pronounced effect on total Li-ion conductivity and activation energy [43,44,56–58]. For pellets made of NSP-synthesized Al-doped pure cubic garnet, total Li-ion conductivity of $4.4 \times 10^{-6} \text{ S cm}^{-1}$ with an activation energy of 0.49 eV has been reported [43].

AC impedance spectroscopy was used to determine the conductivity of the non-infiltrated garnet thin films. The Nyquist and the corresponding Bode plots for the Al-doped garnet thin film recorded at 473 K are shown in Figure 5. From the Nyquist plot (Figure 5a), a strongly depressed semicircle in the high and intermediate frequency range could be seen along with a low frequency tail due to the Li-ion blocking at the gold electrodes, demonstrating that the material under investigation is a Li-ion conductor [43]. The presence of a single semicircle suggests the use of one R-CPE element to fit the impedance data, which could further be confirmed from the Bode plots (Figure 5b,c). Here, R is the resistor and CPE is the constant phase element used to mimic the behavior of an imperfect capacitor. Another CPE connected in series was used to model the capacitive

behavior at low frequencies. The total conductivity of the prepared garnet thin film was determined according to the following equation:

$$\sigma = t/RA$$

where t is the thickness of the electrolyte, R is the resistance obtained from the intercept on the X-axis and A is the area of the sputtered gold electrode. From the fitting, the total conductivity of $4.08 \times 10^{-9} \text{ S cm}^{-1}$ was determined at 473 K. Although the room temperature conductivity of the garnet thin films could not be determined from the impedance measurements due to the high impedances at low temperatures, extrapolation of the Arrhenius plot (Figure 5d) shows that the room temperature conductivity of the Al-doped cubic garnet thin films was of the order of $10^{-13} \text{ S cm}^{-1}$, which is significantly lower than the other garnet thin films previously reported [59–62]. In comparison to the bulk ceramics made of the NSP powder, the low conductivity of such porous films can be well explained due to the following points: (i) reduced sintering temperature (1173 K), (ii) reduced sintering duration (180 min) and (iii) the high porosity and low density of fabricated thin films required to achieve sufficient infiltration. Although high conductivities are desirable, we would like to emphasize that the main focus of this study lies in the formation of a porous network of Li-ion conducting matrix phase, which can be used as the three-dimensional backbone for composite electrolytes and offer continuous Li-ion migration pathways in composite electrolytes; thus, a reduction of the overall conductivity is intrinsic for such porous systems.

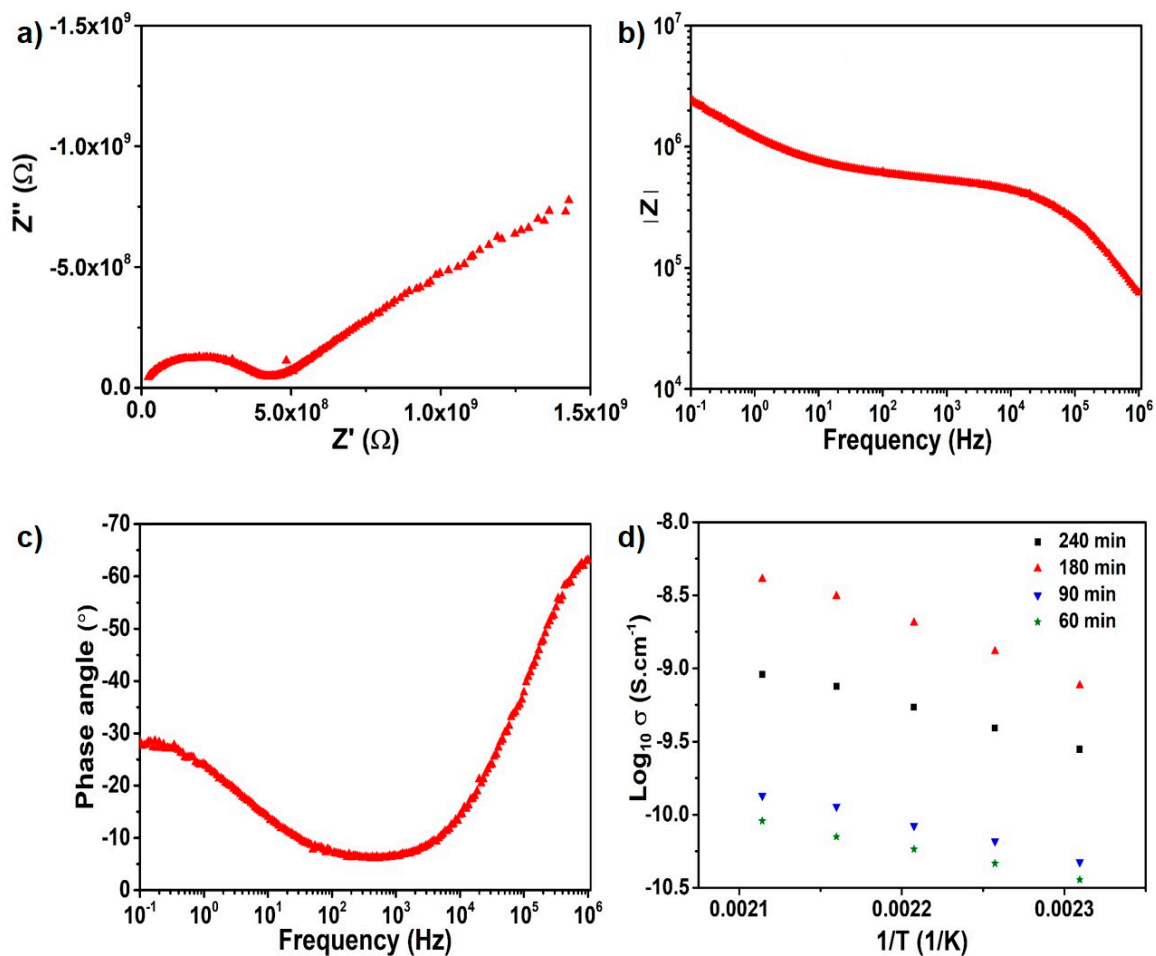


Figure 5. (a) Complex plane plot for Al-doped LLZO garnet thin film recorded at 473 K. (b,c) Respective Bode plots. (d) Arrhenius plot for the Al-doped LLZO garnet thin films sintered at 1173 K at different temperatures.

To assign the R-CPE element to grain or grain boundary contribution, capacitance values were calculated from the following equation:

$$C = CPE^{\frac{1}{n}} R^{1-\frac{1}{n}}$$

where C is the capacitance, and n is the exponential factor. From the fitting, the single RCP element used to fit the impedance data showed a capacitance of an order of 10^{-12} F, which is an indication of grain dominated Li-ion transport [63].

Figure 5d shows the temperature-dependent total ionic conductivity of the garnet thin film, which can be expressed in form of an Arrhenius equation given by $\sigma_{\text{tot}}(T) = \sigma_0 \exp(-E_a/RT)$, where σ_0 is the pre-exponential constant, E_a is the activation energy, R is the molar gas constant and T is the absolute temperature. As seen, the conductivity of the Al-doped cubic garnets was highly dependent on the sintering times. As the annealing temperature increased from 60 min to 180 min, the conductivity was found to increase, which can be explained by an increase of grain growth. However, for the sample annealed for 240 min, the conductivity was found to decrease again, which could be due to the presence of additional impurity phases in the films, confirmed from diffraction data analysis (see Figure S2). For the film annealed for 180 min, an activation energy of 0.75(1) eV was determined from the slope of the Arrhenius plot, which is higher than the NSP-synthesized pellets previously reported (0.49 eV for Al-doped LLZO) [43]. The higher activation energies again originated from lower sintering temperatures compared to that of NSP-synthesized pellets.

For a reasonable understanding of the contributions to the overall conductivity, impedance measurements were also carried out on a thin film of PEO-LiTFSI as a reference system (Figure S4 in Supplementary Information), for which the total ionic conductivity of $3.65 \times 10^{-5} \text{ S cm}^{-1}$ was determined, and the activation energy calculated from the slope of the Arrhenius plot was found to be 0.93(2) eV.

As-prepared porous Al-doped LLZO garnet thin films were infiltrated with the PEO+LiTFSI containing solution in order to achieve filling of the empty voids with the Li-ion conducting polymer, aiming to introduce additional pathways “garnet–polymer–garnet” and to increase the intrinsic accessible surface area for the transport of Li^+ ions. Figure 6 shows the Nyquist and Bode plots of the infiltrated Al-doped LLZO garnet film. Overall conductivities were found to increase by approximately six orders of magnitude as compared to the non-infiltrated films, and impedance measurements could therefore be carried out in a lower temperature range of 298 K and 328 K. As seen from Figure 6a, the complex plane plot clearly shows two semicircles, one at high frequencies followed by another one at intermediate frequencies. At low frequencies, the capacitive behavior due to the Li-ion blocking can be observed. The presence of two semicircles in the Nyquist plot is also complemented by Bode plots, which confirm two different transport processes in the infiltrated films. Therefore, two R-CPE elements connected in series were used to fit the impedance data in the high and mid frequency range, followed by a CPE element to model the low frequency blocking behavior. The total Li-ion conductivity was calculated from the resistance values obtained from the equivalent circuit used and found to be equal to $5.3 \times 10^{-7} \text{ S cm}^{-1}$ at 298 K. The calculated capacitances for the individual R-CPE elements were found to be of the order of 10^{-11} and 10^{-7} F for the first and second R-CPE element, respectively, which are in agreement with the grain and interfacial capacitances [64]. This indicates a strong contribution of Li-ion transport via the garnet network and along the garnet/PEO interface within the incorporated polymer in the infiltrated films.

Figure 6d shows the Arrhenius plot for the infiltrated films. The activation energies were determined from the slope of the Arrhenius plot and were found to be 0.40(1), 0.09(1) and 0.14(1) eV for grain, interface and overall activation energy of the sample, respectively. The first activation energy obtained for the semicircle with bulk capacity corresponded well to what would be expected for bulk grain conduction of garnet-based materials [44], and strongly differed from the activation energy observed for a pure PEO film. The observed activation energy for the second semicircle (which dominates the overall

conductivity) was significantly lower from what has been reported in the literature for composite electrolytes [35,38]. We assume that this lower activation energy observed for the semicircle with a capacity of 10^{-7} F thus might originate mostly from a synergistic effect of the 3D interconnected garnet backbone, providing a continuous interface between the PEO/garnet network. We will detail this explanation in the following.

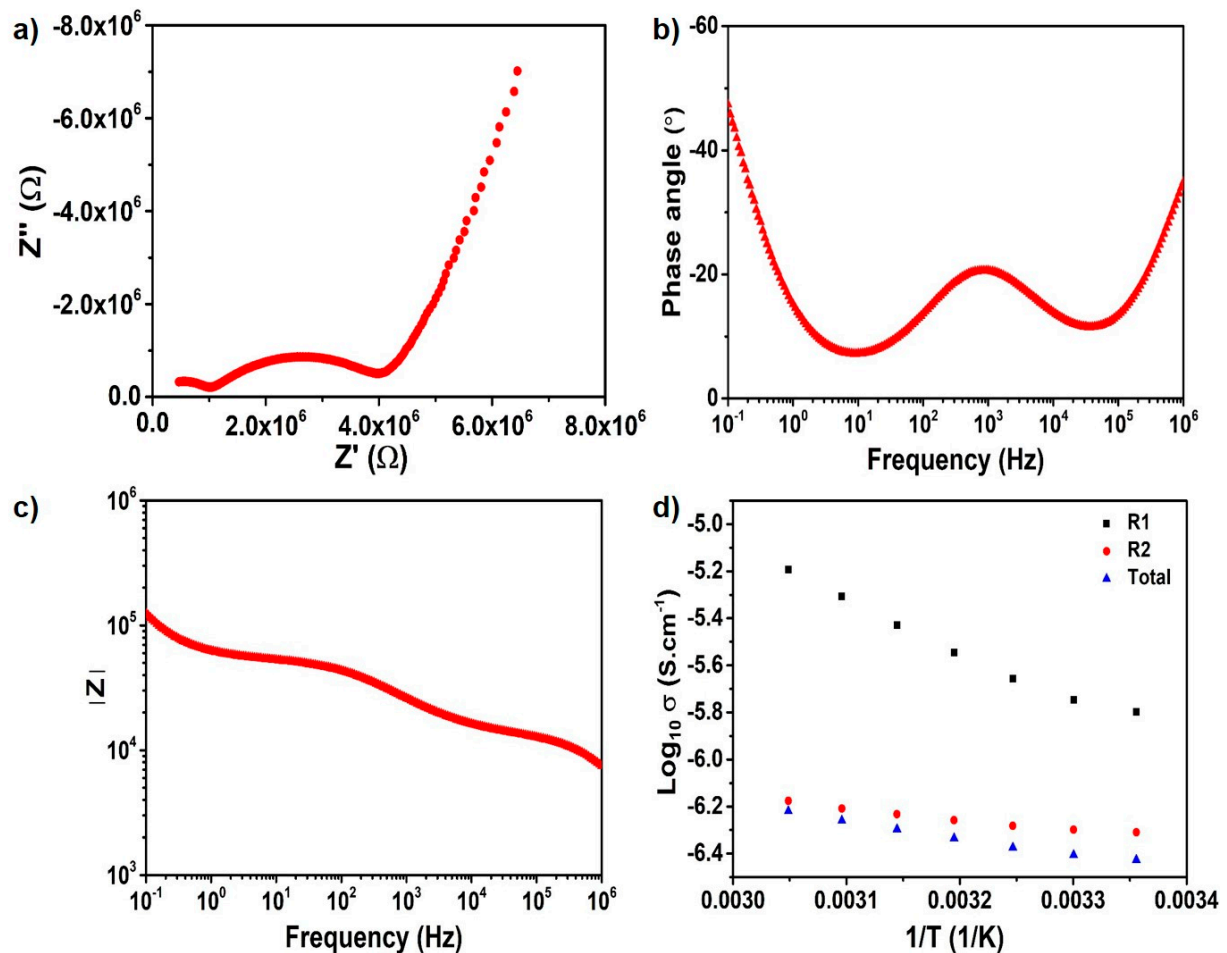


Figure 6. Nyquist plot for the infiltrated Al-doped LLZO garnet thin films measured at 298 K. (a–c) Bode plots corresponding to the complex plane plot measured at 298 K. (d) Arrhenius plot for the infiltrated garnet film measured in the temperature range between 298 K and 328 K (See Figure S1).

For PEO-rich composite electrolytes, i.e., ceramic weight percentages lower than 10%, it is well known that the Li-ion transport takes place via the bulk PEO and along with the ceramic/PEO interface, irrespective of the composition of the ceramic filler [35,41]. The interfacial contribution in such polymer rich composite electrolytes has been known to result in enhanced Li-ion conductivities compared to that of pure polymer electrolytes [31,41]. For an increase of the ceramic weight fraction, agglomeration of the ceramic particles takes place, and conduction also takes place via the ceramic particles [37]; however, transport resistances perpendicular to the garnet-polymer interface are high, which is a limiting factor for accessing the high bulk conductivity.

Thus, it is important to estimate if the film prepared here represents a polymer-rich or a ceramic-rich scenario. Though a precise determination of the thin film density is difficult, it is possible to approximate the ratios of PEO to garnet compared to the composite electrolytes reported previously [30]. Assuming a similar overall ceramic density of 47% [43] as obtained for the sintered NSP powders, this would correspond to the weight ratio between garnet and polymer of 85:15 at the maximum under the assumption that the cavities are fully filled by the polymer.

A continuous and porous ceramic network would be beneficial to take advantage of ceramic/PEO interfacial contribution; the ideal sintered ceramics have strong grain conduction and high surface interactions between the crystallites (Figure 7a). In comparison, the low sintering times and temperatures used here are disadvantageous for creating wide sintering necks between the particles (but necessary to achieve a network that can be infiltrated; Figure 7b,c). Thus, the fact that the porous films show a low conductivity regardless of the high phase purity must be attributed to the existence of narrow sintering necks, which act as bottlenecks for the ionic transport in the porous garnet matrix (see Figure 7c). The increase of conductivity observed in the infiltrated films reported in this article thus might originate from additional contributions from electrically-active garnet/PEO interfaces around the bottlenecks, in agreement with the capacities observed for the second semicircle in the impedance measurement. Thus, the bottlenecks of ionic transport are widened due to the interaction of the polymer with the garnet matrix, increasing the contribution of the garnet matrix on the overall conductivity (Figure 7d).

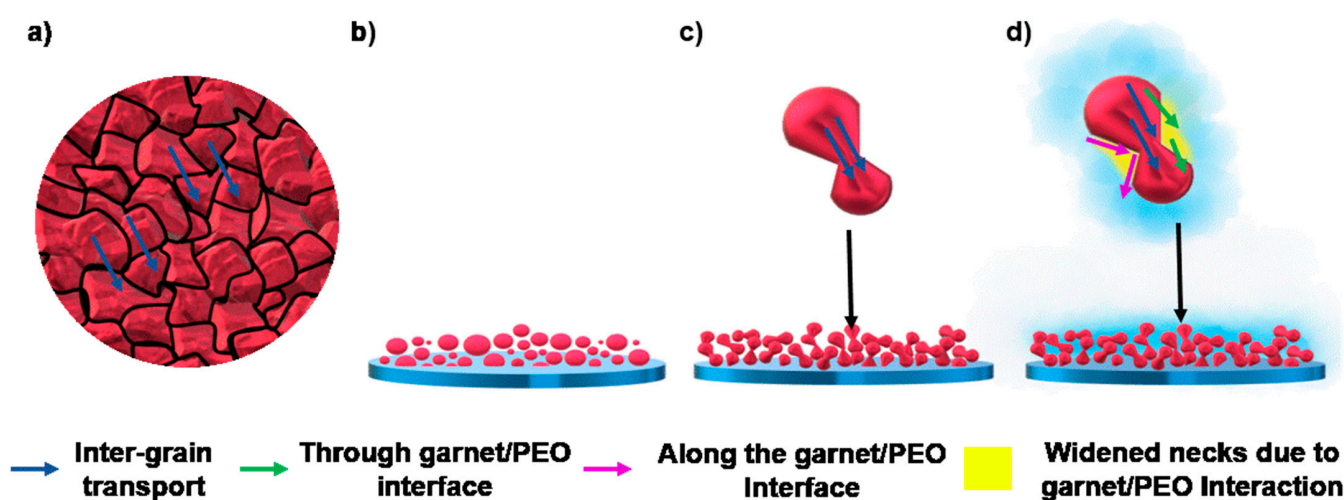


Figure 7. Schematic illustrating (a) Li-ion transport in dense sintered ceramic with large grain size, (b) spin coated NSP powder on the Cu substrate, (c) necking between the particles in the annealed NSP-synthesized garnet powders and (d) Li-ion transport pathways within the infiltrated films.

The intrinsic conductivity of the filler indeed plays a crucial role in ceramic rich composite electrolyte systems [33] by investigating composites of NSP-synthesized garnet particles and PEO+LiTFSI prepared via a solvent-free approach. Within such conventional composite electrolyte membrane preparation, the ceramic fillers would be in mere mechanical contact with each other. In contrast, the approach used here shows the development of connected porous and continuous network. The infiltration of Li-ion conducting PEO not only increases the overall conductivity, but also results in the additional Li-ion transport pathway via the garnet/PEO interface. Further, the conductivity is significantly higher to what would be expected for a composite with the similar garnet to PEO+LiTFSI ratio of particle agglomerates within a polymer matrix ($5.3 \times 10^{-7} \text{ S cm}^{-1}$ vs. $8 \times 10^{-8} \text{ S cm}^{-1}$) [33].

Thus, the main advantage of the porous annealed 3D garnet network would in principle offer higher ionic conductivity than the mechanically contacted garnet filler particles, which are traditionally used in composite electrolytes [14,37]. However, the infiltration may still not be ideal, and smaller degrees of unfilled voids might still exist, which could contribute towards higher impedance. Regardless of these considerations, the conductivity reported here is comparable to those reported in the literature for a 50:50 wt % ratio of PEO to garnet [37]. Thus, though the overall conductivity of the film is not sufficient for achieving a functional solid-state battery, we conclude that infiltrable networks of ion conductors can play an important role in achieving the contribution of the inorganic matrix within composite electrolytes on the overall conduction process.

It is also interesting to put this finding in the context of previous findings. For composite electrolytes, the morphology of the ceramic filler and weight percentages was already discussed to have some impact on the overall conductivity [37]. For low weight fractions of ceramic fillers, nanowire-containing composite electrolytes are shown to improve the ionic conductivities compared to ceramic-free or nanoparticle-containing composites. This was attributed to a higher surface area and suitable directionality of the nanowire morphology, thus affecting the recrystallization kinetics and enhancing Lewis acid–base type interactions [35,41,53]. However, the higher the polymer content, the more difficult it might become to hinder the dendritic growth of lithium. It is well known that garnets offer higher ionic conductivities than the polymer-based electrolytes or composite electrolytes [6]. However, in conventionally mixed ceramic-rich composites, the garnet framework is just a dispersion of more or less loose particles within a polymer-matrix, which leads to high impedances for Li-ion transport at the particle/particle interfaces and has significant grain boundary contribution towards total Li-ion transport. Thus, the morphologies reported here might be suitable for combining the advantageous mechanical properties of the polymers with the beneficial properties of ceramic ion conductors.

We would like to acknowledge that although the conductivities of the composite thin films reported here are too low for their application in ASSBs, an alternative method might be applicable to improve them. For example, using sintering aids during the heat treatment of garnet thin films might provide broader necks between the particles and thus widen the bottlenecks currently encountered in the garnet-based framework; this has been shown to increase the conductivity of the garnets even in conventional dense ceramics [64]. Apart from this, the conductivity can be sufficient for thin film batteries, for which an aspect ratio d/A is of the order of 100–1000 times smaller than for pellet morphologies, and thus the electrolyte can be of reduced conductivity in order to be functional; here the preparation of even thinner porous films in the order of 1–10 μm would be preferable.

4. Conclusions

In this work, we show that porous three-dimensional garnet thin films can be prepared by combining nebulized spray pyrolysis and spin coating. Although the post fabrication heat treatment does not show much influence on the microstructure, it is observed that the ionic conductivity is affected by the annealing duration. Polymer infiltration of the porous garnet films results in increased ionic conductivity by approximately six orders of magnitude, activating the ionic transport pathway through the garnet network. Electrochemical impedance spectroscopy measurements show the contribution of the PEO/garnet interface towards ionic conductivity, which is assigned to providing additional pathways around the sintering necks of the garnet matrix, thus widening the bottlenecks of the ionic conduction pathways. Though the conductivity of the film is low, it might still be sufficient for use within thin film batteries. The additional reduction of thickness will be targeted in a further study.

Further, we emphasize that the porosity of the film might be modified further by the addition of sintering aids or combustible organic compounds, leading to denser or less dense films, respectively.

Supplementary Materials: The following are available online at <https://www.mdpi.com/article/10.3390/ceramics4030031/s1>. Figure S1: (a) Nyquist plot for two different infiltrated cubic Al-doped garnet films measured at 298 K. (b) Temperature dependent Arrhenius plot measured for the two different Al-doped garnet films measured in the temperature range of 298 K to 328 K; Figure S2: Rietveld fit of the X-ray diffractogram of the Al-doped LLZO garnet thin film annealed for 240 min; Figure S3: Cross sectional view of the garnet thin film; Figure S4: Impedance measurements carried out for the PEO thin film at 298 K.

Author Contributions: Conceptualization, O.C. and A.I.W.; methodology, A.I.W.; sample preparation, V.V.; X-ray diffraction, impedance measurements and SEM, A.I.W.; data analysis, A.I.W.; writing—original draft preparation, A.I.W.; writing—review and editing, A.I.W. and O.C.; funding acquisition, O.C. All authors have read and agreed to the published version of the manuscript.

Funding: A.I. Waidha and O. Clemens acknowledge funding within CL551/3-1 by the German Research Foundation (DFG).

Institutional Review Board Statement: Not applicable.

Informed Consent Statement: Not applicable.

Data Availability Statement: Data shown within this manuscript can be obtained from the authors on request.

Conflicts of Interest: The authors declare no conflict of interest.

References

1. Takada, K. Progress and prospective of solid-state lithium batteries. *Acta Mater.* **2013**, *61*, 759–770. [[CrossRef](#)]
2. Shoji, M.; Cheng, E.J.; Kimura, T.; Kanamura, K. Recent progress for all solid state battery using sulfide and oxide solid electrolytes. *J. Phys. D Appl. Phys.* **2019**, *52*, 103001. [[CrossRef](#)]
3. Shen, Y.B.; Zhang, Y.T.; Han, S.J.; Wang, J.W.; Peng, Z.Q.; Chen, L.W. Unlocking the Energy Capabilities of Lithium Metal Electrode with Solid-State Electrolytes. *Joule* **2018**, *2*, 1674–1689. [[CrossRef](#)]
4. Schnell, J.; Günther, T.; Knoche, T.; Vieider, C.; Köhler, L.; Just, A.; Keller, M.; Passerini, S.; Reinhart, G. All-solid-state lithium-ion and lithium metal batteries—Paving the way to large-scale production. *J. Power Sources* **2018**, *382*, 160–175. [[CrossRef](#)]
5. Yao, F.; Pham, D.T.; Lee, Y.H. Carbon-Based Materials for Lithium-Ion Batteries, Electrochemical Capacitors, and Their Hybrid Devices. *ChemSuschem* **2015**, *8*, 2284–2311. [[CrossRef](#)]
6. Zhang, Z.; Shao, Y.; Lotsch, B.; Hu, Y.-S.; Li, H.; Janek, J.; Nazar, L.F.; Nan, C.-W.; Maier, J.; Armand, M.; et al. New horizons for inorganic solid state ion conductors. *Energy Environ. Sci.* **2018**, *11*, 1945–1976. [[CrossRef](#)]
7. Nair, J.R.; Colò, F.; Kazzazi, A.; Moreno, M.; Bresser, D.; Lin, R.; Bella, F.; Meligrana, G.; Fantini, S.; Simonetti, E.; et al. Room temperature ionic liquid (RTIL)-based electrolyte cocktails for safe, high working potential Li-based polymer batteries. *J. Power Sources* **2019**, *412*, 398–407. [[CrossRef](#)]
8. Quartarone, E.; Mustarelli, P.; Magistris, A. PEO-based composite polymer electrolytes. *Solid State Ionics* **1998**, *110*, 1–14. [[CrossRef](#)]
9. Yao, P.; Yu, H.; Ding, Z.; Liu, Y.; Lu, J.; Lavorgna, M.; Wu, J.; Liu, X. Review on Polymer-Based Composite Electrolytes for Lithium Batteries. *Front. Chem.* **2019**, *7*, 522. [[CrossRef](#)]
10. Qian, S.; Chen, H.; Wu, Z.; Li, D.; Liu, X.; Tang, Y.; Zhang, S. Designing Ceramic/Polymer Composite as Highly Ionic Conductive Solid-State Electrolytes. *Batter. Supercaps* **2020**, *4*, 39–59. [[CrossRef](#)]
11. Xue, Z.; He, D.; Xie, X. Poly(ethylene oxide)-based electrolytes for lithium-ion batteries. *J. Mater. Chem. A* **2015**, *3*, 19218–19253. [[CrossRef](#)]
12. Brissot, C.; Rosso, M.; Chazalviel, J.N.; Baudry, P.; Lascaud, S. In situ study of dendritic growth in lithium/PEO-salt/lithium cells. *Electrochim. Acta* **1998**, *43*, 1569–1574. [[CrossRef](#)]
13. Barai, P.; Higa, K.; Srinivasan, V. Lithium dendrite growth mechanisms in polymer electrolytes and prevention strategies. *Phys. Chem. Chem. Phys.* **2017**, *19*, 20493–20505. [[CrossRef](#)]
14. Zhang, J.; Zhao, N.; Zhang, M.; Li, Y.; Chu, P.K.; Guo, X.; Di, Z.; Wang, X.; Li, H. Flexible and ion-conducting membrane electrolytes for solid-state lithium batteries: Dispersion of garnet nanoparticles in insulating polyethylene oxide. *Nano Energy* **2016**, *28*, 447–454. [[CrossRef](#)]
15. Falco, M.; Simari, C.; Ferrara, C.; Nair, J.R.; Meligrana, G.; Bella, F.; Nicotera, I.; Mustarelli, P.; Winter, M.; Gerbaldi, C. Understanding the Effect of UV-Induced Cross-Linking on the Physicochemical Properties of Highly Performing PEO/LiTFSI-Based Polymer Electrolytes. *Langmuir* **2019**, *35*, 8210–8219. [[CrossRef](#)]
16. Thangadurai, V.; Kaack, H.; Weppner, W.J.F. Novel fast lithium ion conduction in garnet-type $\text{Li}_5\text{La}_3\text{M}_2\text{O}_{12}$ (M = Nb, Ta). *J. Am. Ceram. Soc.* **2003**, *86*, 437–440. [[CrossRef](#)]
17. Knauth, P. Inorganic solid Li ion conductors: An overview. *Solid State Ionics* **2009**, *180*, 911–916. [[CrossRef](#)]
18. Sun, C.; Liu, J.; Gong, Y.; Wilkinson, D.P.; Zhang, J. Recent advances in all-solid-state rechargeable lithium batteries. *Nano Energy* **2017**, *33*, 363–386. [[CrossRef](#)]
19. Chen, S.; Xie, D.; Liu, G.; Mwizerwa, J.P.; Zhang, Q.; Zhao, Y.; Xu, X.; Yao, X. Sulfide solid electrolytes for all-solid-state lithium batteries: Structure, conductivity, stability and application. *Energy Storage Mater.* **2018**, *14*, 58–74. [[CrossRef](#)]
20. Balaish, M.; Gonzalez-Rosillo, J.C.; Kim, K.J.; Zhu, Y.; Hood, Z.D.; Rupp, J.L.M. Processing thin but robust electrolytes for solid-state batteries. *Nat. Energy* **2021**, *6*, 227–239. [[CrossRef](#)]
21. Wang, C.; Fu, K.; Kammampata, S.P.; McOwen, D.W.; Samson, A.J.; Zhang, L.; Hitz, G.T.; Nolan, A.M.; Wachsman, E.D.; Mo, Y.; et al. Garnet-Type Solid-State Electrolytes: Materials, Interfaces, and Batteries. *Chem. Rev.* **2020**, *120*, 4257–4300. [[CrossRef](#)]
22. Li, Y.; Wang, Z.; Li, C.; Cao, Y.; Guo, X. Densification and ionic-conduction improvement of lithium garnet solid electrolytes by flowing oxygen sintering. *J. Power Sources* **2014**, *248*, 642–646. [[CrossRef](#)]
23. El-Shinawi, H.; Cussen, E.J.; Corr, S.A. Enhancement of the lithium ion conductivity of Ta-doped $\text{Li}_7\text{La}_3\text{Zr}_2\text{O}_{12}$ by incorporation of calcium. *Dalton Trans.* **2017**, *46*, 9415–9419. [[CrossRef](#)] [[PubMed](#)]
24. Xia, W.; Xu, B.; Duan, H.; Guo, Y.; Kang, H.; Li, H.; Liu, H. Ionic Conductivity and Air Stability of Al-Doped $\text{Li}_7\text{La}_3\text{Zr}_2\text{O}_{12}$ Sintered in Alumina and Pt Crucibles. *ACS Appl. Mater. Interfaces* **2016**, *8*, 5335–5342. [[CrossRef](#)] [[PubMed](#)]

25. Truong, L.; Howard, M.; Clemens, O.; Knight, K.S.; Slater, P.R.; Thangadurai, V. Facile proton conduction in H⁺/Li⁺ ion-exchanged garnet-type fast Li-ion conducting Li₅La₃Nb₂O₁₂. *J. Mater. Chem. A* **2013**, *1*, 13469–13475. [[CrossRef](#)]
26. Galven, C.; Fourquet, J.L.; Crosnier-Lopez, M.P.; Le Berre, F. Instability of the Lithium Garnet Li₇La₃Sn₂O₁₂: Li⁺/H⁺ Exchange and Structural Study. *Chem. Mater.* **2011**, *23*, 1892–1900. [[CrossRef](#)]
27. Zhang, S.; Lee, J.Y.; Hong, L. Visualization of particle distribution in composite polymer electrolyte systems. *J. Power Sources* **2004**, *126*, 125–133. [[CrossRef](#)]
28. Kumar, B.; Scanlon, L.G. Polymer-Ceramic Composite Electrolytes. *J. Power Sources* **1994**, *52*, 261–268. [[CrossRef](#)]
29. Liu, W.; Liu, N.; Sun, J.; Hsu, P.C.; Li, Y.; Lee, H.W.; Cui, Y. Ionic conductivity enhancement of polymer electrolytes with ceramic nanowire fillers. *Nano Lett.* **2015**, *15*, 2740–2745. [[CrossRef](#)]
30. Fu, K.K.; Gong, Y.; Dai, J.; Gong, A.; Han, X.; Yao, Y.; Wang, C.; Wang, Y.; Chen, Y.; Yan, C.; et al. Flexible, solid-state, ion-conducting membrane with 3D garnet nanofiber networks for lithium batteries. *Proc. Natl. Acad. Sci. USA* **2016**, *113*, 7094–7099. [[CrossRef](#)]
31. Zheng, J.; Tang, M.; Hu, Y.Y. Lithium Ion Pathway within Li₇La₃Zr₂O₁₂-Polyethylene Oxide Composite Electrolytes. *Angew. Chem. Int. Ed. Engl.* **2016**, *55*, 12538–12542. [[CrossRef](#)]
32. Bae, J.; Li, Y.; Zhang, J.; Zhou, X.; Zhao, F.; Shi, Y.; Goodenough, J.B.; Yu, G. A 3D Nanostructured Hydrogel-Framework-Derived High-Performance Composite Polymer Lithium-Ion Electrolyte. *Angew. Chem. Int. Ed. Engl.* **2018**, *57*, 2096–2100. [[CrossRef](#)]
33. Waidha, A.I.; Ferber, T.; Donzelli, M.; Hosseinpourkahvaz, N.; Vanita, V.; Dirnberger, K.; Ludwigs, S.; Hausbrand, R.; Jaegermann, W.; Clemens, O. Compositional Dependence of Li-Ion Conductivity in Garnet-Rich Composite Electrolytes for All-Solid-State Lithium-Ion Batteries-Toward Understanding the Drawbacks of Ceramic-Rich Composites. *ACS Appl. Mater. Interfaces* **2021**. [[CrossRef](#)] [[PubMed](#)]
34. Falco, M.; Castro, L.; Nair, J.R.; Bella, F.; Bardé, F.; Meligrana, G.; Gerbaldi, C. UV-Cross-Linked Composite Polymer Electrolyte for High-Rate, Ambient Temperature Lithium Batteries. *ACS Appl. Energy Mater.* **2019**, *2*, 1600–1607. [[CrossRef](#)]
35. Zhu, P.; Yan, C.; Dirican, M.; Zhu, J.; Zang, J.; Selvan, R.K.; Chung, C.-C.; Jia, H.; Li, Y.; Kiyak, Y.; et al. Li_{0.33}La_{0.557}TiO₃ ceramic nanofiber-enhanced polyethylene oxide-based composite polymer electrolytes for all-solid-state lithium batteries. *J. Mater. Chem. A* **2018**, *6*, 4279–4285. [[CrossRef](#)]
36. Zagorski, J.; del Amo, J.M.L.; Cordill, M.J.; Aguesse, F.; Buannic, L.; Llordes, A. Garnet-Polymer Composite Electrolytes: New Insights on Local Li-Ion Dynamics and Electrodeposition Stability with Li Metal Anodes. *ACS Appl. Energy Mater.* **2019**, *2*, 1734–1746. [[CrossRef](#)]
37. Chen, L.; Li, Y.; Li, S.-P.; Fan, L.-Z.; Nan, C.-W.; Goodenough, J.B. PEO/garnet composite electrolytes for solid-state lithium batteries: From “ceramic-in-polymer” to “polymer-in-ceramic”. *Nano Energy* **2018**, *46*, 176–184. [[CrossRef](#)]
38. Zekoll, S.; Marriner-Edwards, C.; Hekselman, A.K.O.; Kasemchainan, J.; Kuss, C.; Armstrong, D.E.J.; Cai, D.Y.; Wallace, R.J.; Richter, F.H.; Thijssen, J.H.J.; et al. Hybrid electrolytes with 3D bicontinuous ordered ceramic and polymer microchannels for all-solid-state batteries. *Energy Environ. Sci.* **2018**, *11*, 185–201. [[CrossRef](#)]
39. Keller, M.; Appetecchi, G.B.; Kim, G.-T.; Sharova, V.; Schneider, M.; Schuhmacher, J.; Roters, A.; Passerini, S. Electrochemical performance of a solvent-free hybrid ceramic-polymer electrolyte based on Li₇La₃Zr₂O₁₂ in P(EO)₁₅LiTFSI. *J. Power Sources* **2017**, *353*, 287–297. [[CrossRef](#)]
40. Hitz, G.T.; McOwen, D.W.; Zhang, L.; Ma, Z.; Fu, Z.; Wen, Y.; Gong, Y.; Dai, J.; Hamann, T.R.; Hu, L.; et al. High-rate lithium cycling in a scalable trilayer Li-garnet-electrolyte architecture. *Mater. Today* **2019**, *22*, 50–57. [[CrossRef](#)]
41. Yang, T.; Zheng, J.; Cheng, Q.; Hu, Y.Y.; Chan, C.K. Composite Polymer Electrolytes with Li₇La₃Zr₂O₁₂ Garnet-Type Nanowires as Ceramic Fillers: Mechanism of Conductivity Enhancement and Role of Doping and Morphology. *ACS Appl. Mater. Interfaces* **2017**, *9*, 21773–21780. [[CrossRef](#)] [[PubMed](#)]
42. Xue, W.; Yang, Y.; Yang, Q.; Liu, Y.; Wang, L.; Chen, C.; Cheng, R. The effect of sintering process on lithium ionic conductivity of Li_{6.4}Al_{0.2}La₃Zr₂O₁₂ garnet produced by solid-state synthesis. *RSC Adv.* **2018**, *8*, 13083–13088. [[CrossRef](#)]
43. Djenadic, R.; Botros, M.; Benel, C.; Clemens, O.; Indris, S.; Choudhary, A.; Bergfeldt, T.; Hahn, H. Nebulized spray pyrolysis of Al-doped Li₇La₃Zr₂O₁₂ solid electrolyte for battery applications. *Solid State Ionics* **2014**, *263*, 49–56. [[CrossRef](#)]
44. Botros, M.; Djenadic, R.; Clemens, O.; Moller, M.; Hahn, H. Field assisted sintering of fine-grained Li_{7-3x}La₃Zr₂Al_xO₁₂ solid electrolyte and the influence of the microstructure on the electrochemical performance. *J. Power Sources* **2016**, *309*, 108–115. [[CrossRef](#)]
45. Huo, H.; Luo, J.; Thangadurai, V.; Guo, X.; Nan, C.-W.; Sun, X. Li₂CO₃: A Critical Issue for Developing Solid Garnet Batteries. *ACS Energy Lett.* **2019**, 252–262. [[CrossRef](#)]
46. *Topas V4.2, General Profile and Structure Analysis Software for Powder Diffraction Data, User's Manual*; Bruker AXS: Karlsruhe, Germany, 2008.
47. Cheary, R.W.; Coelho, A.A.; Cline, J.P. Fundamental Parameters Line Profile Fitting in Laboratory Diffractometers. *J. Res. Natl. Inst. Stand. Technol.* **2004**, *109*, 1–25. [[CrossRef](#)]
48. Johnson, D. *ZView: A Software Program for IES Analysis, Version 2.8*; Scribner Associates Inc.: Southern Pines, NC, USA, 2002; p. 200.
49. Chen, R.J.; Huang, M.; Huang, W.Z.; Shen, Y.; Lin, Y.H.; Nan, C.W. Sol-gel derived Li-La-Zr-O thin films as solid electrolytes for lithium-ion batteries. *J. Mater. Chem. A* **2014**, *2*, 13277–13282. [[CrossRef](#)]

50. Bitzer, M.; Van Gestel, T.; Uhlenbruck, S.; Peter, B.H. Sol-gel synthesis of thin solid $\text{Li}_7\text{La}_3\text{Zr}_2\text{O}_{12}$ electrolyte films for Li-ion batteries. *Thin Solid Films* **2016**, *615*, 128–134. [[CrossRef](#)]
51. Waidha, A.I.; Lepple, M.; Wissel, K.; Benes, A.; Wollstadt, S.; Slater, P.R.; Fortes, A.D.; Clemens, O. Synthesis, structure and electrical conductivity of a new perovskite type barium cobaltate $\text{Ba Co O}_{1.80} (\text{O H})_{0.86}$. *Dalton Trans.* **2018**, *47*, 11136–11145. [[CrossRef](#)]
52. Waidha, A.I.; Ni, L.; Ali, J.; Lepple, M.; Donzelli, M.; Dasgupta, S.; Wollstadt, S.; Alff, L.; Kramm, U.I.; Clemens, O. Synthesis of bifunctional $\text{Ba Fe}_{1-x} \text{Co}_x \text{O}_{3-y-\delta} (\text{OH})_y$ catalysts for the oxygen reduction reaction and oxygen evolution reaction. *J. Mater. Chem. A* **2020**, *8*, 616–625. [[CrossRef](#)]
53. Liu, W.; Lin, D.; Sun, J.; Zhou, G.; Cui, Y. Improved Lithium Ionic Conductivity in Composite Polymer Electrolytes with Oxide-Ion Conducting Nanowires. *ACS Nano* **2016**, *10*, 11407–11413. [[CrossRef](#)]
54. Wollstadt, S.; Clemens, O. On the Impact of the Degree of Fluorination on the ORR Limiting Processes within Iron Based Catalysts: A Model Study on Symmetrical Films of Barium Ferrate. *Materials* **2020**, *13*, 2532. [[CrossRef](#)]
55. Huang, M.; Liu, T.; Deng, Y.; Geng, H.; Shen, Y.; Lin, Y.; Nan, C.-W. Effect of sintering temperature on structure and ionic conductivity of $\text{Li}_{7-x}\text{La}_3\text{Zr}_2\text{O}_{12-0.5x}$ ($x = 0.5\sim 0.7$) ceramics. *Solid State Ionics* **2011**, *204–205*, 41–45. [[CrossRef](#)]
56. Zhang, Y.H.; Chen, F.; Tu, R.; Shen, Q.; Zhang, L.M. Field assisted sintering of dense Al-substituted cubic phase $\text{Li}_7\text{La}_3\text{Zr}_2\text{O}_{12}$ solid electrolytes. *J. Power Sources* **2014**, *268*, 960–964. [[CrossRef](#)]
57. Sakamoto, J.; Rangasamy, E.; Kim, H.; Kim, Y.; Wolfenstine, J. Synthesis of nano-scale fast ion conducting cubic $\text{Li}_7\text{La}_3\text{Zr}_2\text{O}_{12}$. *Nanotechnology* **2013**, *24*, 424005. [[CrossRef](#)]
58. El Shinawi, H.; Janek, J. Stabilization of cubic lithium-stuffed garnets of the type “ $\text{Li}_7\text{La}_3\text{Zr}_2\text{O}_{12}$ ” by addition of gallium. *J. Power Sources* **2013**, *225*, 13–19. [[CrossRef](#)]
59. Loho, C.; Djenadic, R.; Bruns, M.; Clemens, O.; Hahn, H. Garnet-Type $\text{Li}_7\text{La}_3\text{Zr}_2\text{O}_{12}$ Solid Electrolyte Thin Films Grown by CO_2 -Laser Assisted CVD for All-Solid-State Batteries. *J. Electrochem. Soc.* **2016**, *164*, A6131–A6139. [[CrossRef](#)]
60. Wolfenstine, J.; Rangasamy, E.; Allen, J.L.; Sakamoto, J. High conductivity of dense tetragonal $\text{Li}_7\text{La}_3\text{Zr}_2\text{O}_{12}$. *J. Power Sources* **2012**, *208*, 193–196. [[CrossRef](#)]
61. Tadanaga, K.; Egawa, H.; Hayashi, A.; Tatsumisago, M.; Mosa, J.; Aparicio, M.; Duran, A. Preparation of lithium ion conductive Al-doped $\text{Li}_7\text{La}_3\text{Zr}_2\text{O}_{12}$ thin films by a sol-gel process. *J. Power Sources* **2015**, *273*, 844–847. [[CrossRef](#)]
62. Lobe, S.; Dellen, C.; Finsterbusch, M.; Gehrke, H.G.; Sebold, D.; Tsai, C.L.; Uhlenbruck, S.; Guillon, O. Radio frequency magnetron sputtering of $\text{Li}_7\text{La}_3\text{Zr}_2\text{O}_{12}$ thin films for solid-state batteries. *J. Power Sources* **2016**, *307*, 684–689. [[CrossRef](#)]
63. Irvine, J.T.S.; Sinclair, D.C.; West, A.R. Electroceramics: Characterization by Impedance Spectroscopy. *Adv. Mater.* **1990**, *2*, 132–138. [[CrossRef](#)]
64. Rosero-Navarro, N.C.; Yamashita, T.; Miura, A.; Higuchi, M.; Tadanaga, K. Effect of Sintering Additives on Relative Density and Li-ion Conductivity of Nb-Doped $\text{Li}_7\text{La}_3\text{Zr}_2\text{O}_{12}$ Solid Electrolyte. *J. Am. Ceram. Soc.* **2017**, *100*, 276–285. [[CrossRef](#)]